HNUE JOURNAL OF SCIENCE
Natural Sciences 2025, Volume 70, Issue 2, pp. 78-90
This paper is available online at http://hnuejs.edu.vn/ns
DOI: 10.18173/2354-1059.2025-0023

INVESTIGATION OF THE PROPERTIES AND ENHANCED PHOTOCATALYTIC ACTIVITY OF Bi_2WO_6/g-C_3N_4 COMPOSITE MATERIALS

Luc Huy Hoang [1,2], Tu Nhu Hanh[2], Vu Quoc Trung[2] and Nguyen Dang Phu[3,*]
[1]*Institute of Natural Sciences, Hanoi National University of Education, Hanoi city, Vietnam*
[2]*Faculty of Physics, Hanoi National University of Education, Hanoi city, Vietnam*
[3]*Faculty of Electronics and Telecommunications, University of Engineering and Technology, Vietnam National University, Hanoi city, Vietnam*
[*]Corresponding author: Nguyen Dang Phu, e-mail: phund@vnu.edu.vn

Received May 14, 2025. Revised June 20, 2025. Accepted June 30, 2025.

Abstract. Bi_2WO_6/g-C_3N_4 composite materials with varying g-C_3N_4 weight fractions (5%, 10%, 15% and 20%) were successfully synthesized using a combined microwave-hydrothermal method. The structural, morphological, and optical properties of the composites were characterized by X-ray diffraction (XRD), scanning electron microscopy (SEM), UV-Vis absorption spectroscopy, and photoluminescence (PL) spectroscopy. Photocatalytic performance was evaluated by the degradation of Rhodamine B (RhB) under simulated sunlight, employing a cutoff filter to eliminate wavelengths below 400 nm. The incorporation of g-C_3N_4 into Bi_2WO_6 was found to significantly modify its morphology and enhance its optical absorption. All composite samples exhibited superior photocatalytic activity compared to pure Bi_2WO_6, with the 10 wt% g-C_3N_4 composite achieving the highest degradation rate, approximately seven times that of pristine Bi_2WO_6. This enhancement is primarily attributed to the formation of a Z-scheme heterojunction between Bi_2WO_6 and g-C_3N_4, which promotes efficient charge separation and suppresses electron-hole recombination via electron trap centers.

Keywords: composite materials, photocatalytic activity, hydrothermal method, semiconductor, heterojunction.

1. Introduction

Bismuth tungstate (Bi_2WO_6) has emerged as a promising visible-light-driven photocatalyst owing to its narrow band gap and excellent chemical stability [1]-[5]. These properties make it a potential candidate for environmental remediation applications such as wastewater treatment. However, its practical performance is hindered by the rapid

recombination of photogenerated electron-hole pairs, which significantly reduces its photocatalytic efficiency [6], [7]. To address this limitation, various strategies have been explored to enhance the photocatalytic activity of Bi_2WO_6, including elemental doping and composite formation [8]-[10]. Elemental doping has been achieved by substituting Bi with metal ions such as Ag [11] or Fe [10], replacing W with Mo [12], or introducing nonmetal dopants such as fluorine and nitrogen [13], [14]. Another effective approach involves constructing heterojunctions by combining Bi_2WO_6 with other semiconductors e.g., $BiVO_4$ [15], [16], TiO_2 [17], [18], MoS_2 [19], and g-C_3N_4 [20], [21].

Among various semiconductors, graphitic carbon nitride (g-C_3N_4) stands out due to its visible-light responsiveness, thermal stability and tunable electronic structure. When coupled with Bi_2WO_6 - an n-type semiconductor - the resulting Bi_2WO_6/g-C_3N_4 composite can form a heterojunction that facilitates effective charge separation and suppresses electron–hole recombination, thereby enhancing photocatalytic efficiency. Depending on the band alignment and interfacial structure, this heterostructure may operate via type-II, Z-scheme, or S-scheme mechanisms. Notably, heterojunction formation is highly sensitive to synthesis conditions, which influence morphology, crystallinity, and interfacial contact [21]-[25]. Although both microwave-assisted and hydrothermal methods have been individually employed in semiconductor synthesis, their combination remains underexplored. The microwave-assisted hydrothermal method offers synergistic advantages: uniform, rapid heating by microwaves and controlled crystal growth under hydrothermal conditions. This dual approach has shown promise for generating nanostructures with enhanced photocatalytic activity via improved interfacial contact and defect engineering.

In this study, Bi_2WO_6/g-C_3N_4 composites with varying g-C_3N_4 content (5%, 10%, 15% and 20% by weight) were synthesized using the combined microwave-hydrothermal route. This strategy promotes the formation of a direct Z-scheme heterojunction, which effectively improves charge-carrier separation while retaining strong redox potentials. The pristine Bi_2WO_6 was also synthesized under identical conditions for comparison. The structural, morphological**,** and optical characteristics of the resulting materials were systematically analyzed, and their photocatalytic performance under simulated visible light was evaluated. Furthermore, a comparative analysis with previous reports was conducted to demonstrate the advantages of the adopted synthetic approach.

2. Content

2.1. Experimental methods

2.1.1. Chemicals and experimental equipment

Urea sourced from China was used as the precursor for synthesizing graphitic carbon nitride (g-C_3N_4), while bismuth nitrate pentahydrate ($Bi(NO_3)_3 \cdot 5H_2O$) and sodium tungstate dihydrate ($Na_2WO_4 \cdot 2H_2O$), both obtained from Sigma-Aldrich, were employed as precursors for Bi_2WO_6 synthesis. The microwave system was adapted from a commercially available microwave oven with minor modifications to suit experimental requirements. A Nabertherm TR240 oven was employed for the heating process during the hydrothermal treatment.

2.1.2. Synthesis of g-C_3N_4

g-C_3N_4 was synthesized via the thermal polymerization of urea in ambient air. Specifically, 5.0 g of urea was placed in a covered crucible and calcined at 500 °C for 5 h in a Nabertherm LH120 muffle furnace, using a heating rate of 10 °C min^{-1}. The resulting yellow powder was collected and used without further purification.

2.1.3. Synthesis of Bi_2WO_6/g-C_3N_4 composite

The Bi_2WO_6/g-C_3N_4 composites were synthesized via a combined microwave-assisted hydrothermal method. Initially, 2.5 mmol of $Na_2WO_4 \cdot 2H_2O$ and 5 mmol of $Bi(NO_3)_3 \cdot 5H_2O$ were dissolved in 100 mL of deionized water and stirred for 30 min. Subsequently, the desired amount of pre-synthesized g-C_3N_4 was added to achieve a target weight fraction of 0%, 5%, 10%, 15% or 20% relative to Bi_2WO_6. The mixture was ultrasonically treated for 30 min to ensure homogeneous dispersion. The suspension was then transferred to a 150 mL round-bottom flask and irradiated with microwaves at 750 W for 20 min. Following this step, the suspension was immediately transferred to a 100 mL Teflon-lined autoclave and subjected to hydrothermal treatment at 160 °C for 8 h. After cooling naturally to room temperature, the product was collected by centrifugation, washed four times with deionized water, and dried at 70 °C. The resulting powders - each corresponding to a specific g-C_3N_4 content - were labeled as listed in Table 1.

Table 1. Notation of Bi_2WO_6/g-C_3N_4 samples synthesized with different g-C_3N_4 fractions

Samples	Pristine Bi_2WO_6	Bi_2WO_6/ g-C_3N_4 with 5 wt% g-C_3N_4	Bi_2WO_6/ g-C_3N_4 with 10 wt% g-C_3N_4	Bi_2WO_6/ g-C_3N_4 with 15 wt% g-C_3N_4	Bi_2WO_6/ g-C_3N_4 with 20 wt% g-C_3N_4
Notation	Bi_2WO_6	5% g-C_3N_4	10% g-C_3N_4	15% g-C_3N_4	20% g-C_3N_4

2.1.4. Material characterization methods

The crystalline phases of the synthesized materials were identified using X-ray diffraction (XRD; Bruker D5005). The morphology of the samples was observed by scanning electron microscopy (SEM; Hitachi S-4800). The optical absorption properties were studied by UV-Vis diffuse reflectance spectroscopy (DRS; Jasco V-670). The specific surface area was measured by the Brunauer-Emmett-Teller (BET) method using a Micromeritics TriStar 3000 instrument. Photoluminescence (PL) spectra were recorded on a Horiba FluoroMax-4 spectrofluorometer, excited by a 325 nm He–Cd laser.

2.1.5. Experimental evaluation of photocatalytic properties of the materials

Photocatalytic performance was evaluated by monitoring the degradation of Rhodamine B (RhB) under visible-light irradiation. A 300 W xenon lamp equipped with a cutoff filter ($\lambda < 400$ nm) was used to simulate sunlight. In each experiment, 0.10 g of photocatalyst was dispersed in 100 mL of 10^{-5} M RhB solution. The mixture was stirred in the dark for 3 h to reach adsorption-desorption equilibrium. Upon illumination, 5 mL aliquots were withdrawn every 30 min, centrifuged to remove catalyst particles, and analyzed by UV-Vis spectroscopy. Photodegradation efficiency was determined by tracking the decrease in absorbance at approximately 560 nm, corresponding to the characteristic RhB peak.

2.2. Results and discussion

Figure 1a shows the XRD patterns of pristine Bi_2WO_6, pristine g-C_3N_4, and Bi_2WO_6/g-C_3N_4 composites with 5%, 10%, 15% and 20% g-C_3N_4. The g-C_3N_4 sample displays two characteristic diffraction peaks at 2θ = 27.4° and ≈ 13°, corresponding to the (002) and (100) planes of the graphitic carbon nitride structure, in agreement with JCPDS 87-1526 [26]. These peaks confirm the successful synthesis of g-C_3N_4.

For both pristine Bi_2WO_6 and the composite samples, distinct diffraction peaks appear at 2θ = 28.3°, 32.7°, 47.1°, 55.9° and 58.2°, which can be indexed to the (131), (200), (202), (113) and (262) planes of orthorhombic Bi_2WO_6, consistent with its known crystal structure. The absence of additional peaks in the composite samples indicates that the Bi_2WO_6 crystal phase remains intact after compositing with g-C_3N_4.

Interestingly, no diffraction peaks attributable to g-C_3N_4 are observed in the composites. This is likely due to the weak and broad nature of the g-C_3N_4 signals, which are overshadowed by the more intense Bi_2WO_6 peaks, particularly at low g-C_3N_4 loadings. Similar observations have been reported previously, where low g-C_3N_4 content renders its diffraction signals undetectable in composite XRD patterns [27].

A detailed analysis of the diffraction peaks at specific 2θ angles, particularly the peak at 28.30° (Figure 1b), reveals no observable shift. This indicates that incorporation of g-C_3N_4 does not significantly affect the crystal structure of the Bi_2WO_6 host material.

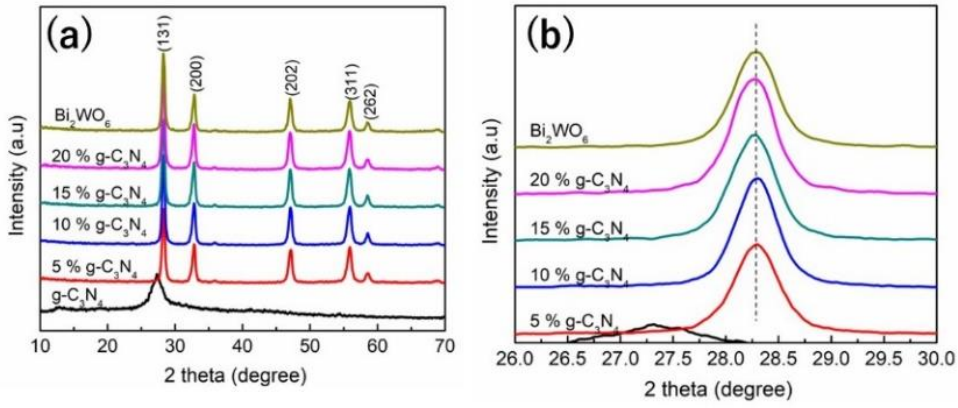

Figure 1. XRD patterns of pristine Bi_2WO_6, Bi_2WO_6/g-C_3N_4 composites with 5%, 10%, 15%, 20% g-C_3N_4, and pure g-C_3N_4 (a); enlarged view of the (131) peak at 28.30° for the composites with varying g-C_3N_4 contents (b)

Figure 2 presents SEM images of (a) pristine Bi_2WO_6, (b) a Bi_2WO_6/g-C_3N_4 composite containing 10 wt% g-C_3N_4, and (c) pure g-C_3N_4. The SEM image of g-C_3N_4 (Figure 2c) reveals its characteristic porous, layered morphology, typical of graphitic carbon nitride. In contrast, the pristine Bi_2WO_6 sample (Figure 2a) consists of plate-like crystallites aggregated into flower-like microscale structures, with clusters several micrometers in size. For the Bi_2WO_6/g-C_3N_4 composite with 10 wt% g-C_3N_4 (Figure 2b), the morphology changes significantly: the Bi_2WO_6 plates are smaller, more randomly oriented, and less aggregated, resulting in the absence of the distinct flower-like structure observed in pristine Bi_2WO_6.

These morphological differences can be attributed to the presence of g-C_3N_4 during synthesis. As Bi_2WO_6 nucleates and grows, the g-C_3N_4 sheets provide a scaffold that hinders the self-assembly of Bi_2WO_6 into tightly packed clusters. Instead, the Bi_2WO_6 crystallites distribute more uniformly across the g-C_3N_4 layers, leading to a more open, porous structure. In addition to morphological analysis, the specific surface area of the samples was measured by the BET method. As summarized in Table 2, pure g-C_3N_4 exhibits the highest surface area, while pristine Bi_2WO_6 shows the lowest. Notably, the surface area of the composites increases with g-C_3N_4 content. This enhancement in surface area is beneficial for photocatalysis, as it provides more active sites and improves interactions between the photocatalyst and pollutant molecules, thereby enhancing photocatalytic performance.

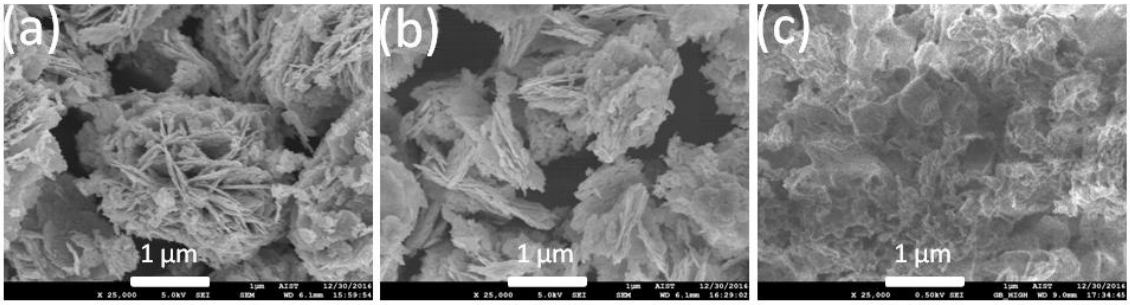

Figure 2. SEM images of (a) pristine Bi_2WO_6, (b) Bi_2WO_6/g-C_3N_4 composite with 10% g-C_3N_4, and (c) pure g-C_3N_4

Figure 3a shows the UV-Vis diffuse reflectance spectra of pristine Bi_2WO_6, Bi_2WO_6/g-C_3N_4 composites with varying g-C_3N_4 contents (5%, 10%, 15% and 20%), and pure g-C_3N_4. The pristine Bi_2WO_6 sample has an absorption edge around 430 nm, characteristic of its visible-light absorption. In contrast, pure g-C_3N_4 shows a red-shifted absorption edge near 500 nm. Notably, the Bi_2WO_6/g-C_3N_4 composites display absorption edges that gradually shift toward longer wavelengths with increasing g-C_3N_4 content, indicating a narrowing of the effective bandgap as the material's optical response approaches that of g-C_3N_4. Additionally, an enhanced baseline absorption in the 500 - 800 nm range is observed for the composites but is absent in pristine Bi_2WO_6. This broader absorption suggests improved light-harvesting capabilities due to synergistic interactions between the two components. To quantify the optical bandgap, the Kubelka-Munk transformation was applied to the reflectance spectra (Figure 3b). The extracted bandgap values are summarized in Table 2. The data clearly indicate that the optical band gaps of the Bi_2WO_6/g-C_3N_4 composites are significantly reduced compared to those of the individual materials, confirming enhanced visible-light absorption. The observation that the composites display a single red-shifted absorption edge, rather than a simple overlay of the spectra of Bi_2WO_6 and g-C_3N_4, suggests the formation of a well-integrated heterojunction. This interfacial coupling likely facilitates efficient charge transfer and separation, thereby improving photocatalytic performance.

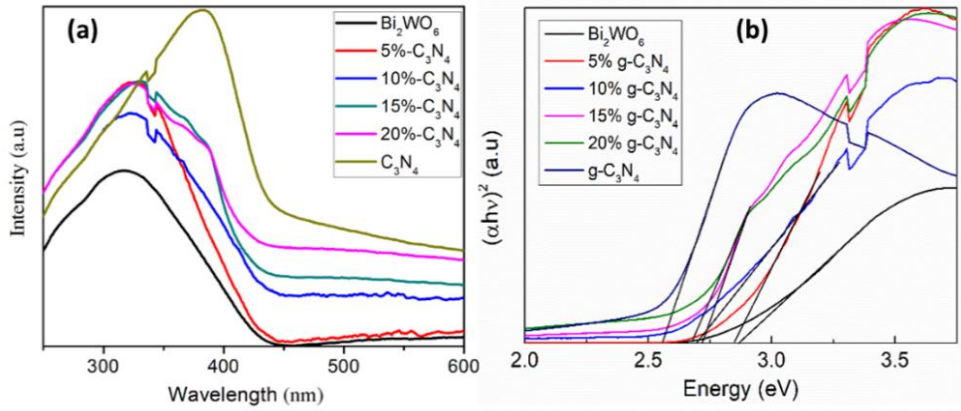

Figure 3. (a) UV-Vis diffuse reflectance spectra and (b) corresponding Kubelka-Munk plots for pristine Bi_2WO_6, pure g-C_3N_4, and Bi_2WO_6/g-C_3N_4 composites containing 5%, 10%, 15%, and 20% g-C_3N_4 by weight

The photocatalytic performance of the prepared samples was evaluated by monitoring the degradation of Rhodamine B (RhB) under visible-light irradiation ($\lambda > 400$ nm). As shown in Figure 4a, the RhB concentration determined by measuring the absorbance at 550 nm decreases progressively with irradiation time in the presence of both Bi_2WO_6/g-C_3N_4 composites and pristine Bi_2WO_6. While all samples exhibit photocatalytic activity under visible light, the composites demonstrate markedly enhanced performance compared to pristine Bi_2WO_6. The degradation efficiency depends on the g-C_3N_4 content: among the tested compositions, the sample containing 10 wt % g-C_3N_4 shows the most efficient behavior, achieving nearly complete degradation of a 10 ppm RhB solution within 60 min. In contrast, pristine Bi_2WO_6 displays significantly lower degradation under identical conditions. These results highlight the beneficial role of g-C_3N_4 in enhancing the photocatalytic activity of the Bi_2WO_6-based composites under visible-light illumination.

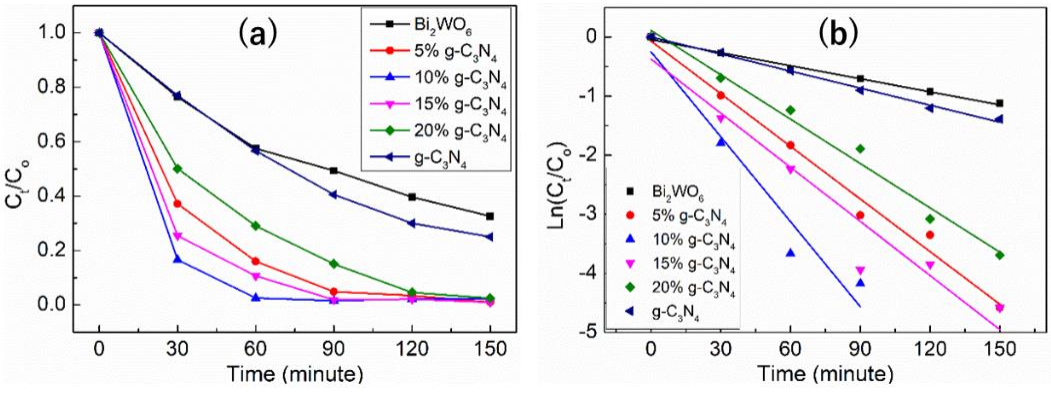

Figure 4. (a) Decolorization of RhB (decrease in 550 nm peak intensity) as a function of irradiation time for Bi_2WO_6/g-C_3N_4 composites under visible light; (b) Corresponding first-order kinetic plots for RhB degradation with each sample

To gain deeper insight into the degradation process, the reaction kinetics were analyzed using the Langmuir-Hinshelwood model. The RhB degradation was fitted to a pseudo-first-order kinetic equation: $\ln(C_t/C_0) = k't$, where C_0 is the initial dye concentration, C_t is the concentration at time t, and k' is the apparent first-order rate constant. Figure 4b presents the linearized kinetic plots for each sample, and the corresponding k' values are listed in Table 2. Among all the samples, the Bi_2WO_6/g-C_3N_4 composite with 10% g-C_3N_4 exhibits the highest rate constant, approximately seven times greater than that of pristine Bi_2WO_6. Interestingly, this composite does not possess the highest specific surface area, indicating that the enhanced activity is not solely due to increased surface area. Instead, the significant improvement can be attributed to the formation of an effective heterojunction between Bi_2WO_6 and g-C_3N_4, which facilitates charge separation and transfer. Additionally, the incorporation of g-C_3N_4 may introduce surface defects, such as oxygen vacancies, which further enhance photocatalytic performance by suppressing charge recombination and improving visible-light absorption.

Table 2. Band gap, specific area and RhB degradation rate constants for Bi_2WO_6/g-C_3N_4 composites with various g-C_3N_4 contents

Samples	**Pristine Bi_2WO_6**	**5% g-C_3N_4**	**10% g-C_3N_4**	**15% g-C_3N_4**	**20% g-C_3N_4**	**g-C_3N_4**
Band gap (eV)	2.87	2.85	2.70	2.70	2.67	2.56
Specific surface area (m^2/g)	15.37	16.01	18.14	20.06	21.76	83.08
RhB degradation rate k′ (min^{-1})	0.0074	0.0297	0.0479	0.0305	0.0250	0.0096

Figure 5 shows the photoluminescence (PL) spectra of pristine Bi_2WO_6, pure g-C_3N_4, and Bi_2WO_6/g-C_3N_4 composites with 5%, 10%, 15%, and 20% g-C_3N_4. The results indicate that pristine Bi_2WO_6 exhibits a strong emission peak around 544 nm, which is attributed to the radiative transition from the Bi 6s/O 2p hybrid orbitals in the valence band to the W 5d orbital in the conduction band of the $[WO_6]^{2-}$ complex [25]. In contrast, all Bi_2WO_6/g-C_3N_4 composites show significantly reduced PL intensity compared to pristine Bi_2WO_6, indicating a lower recombination rate of photoexcited electron-hole pairs. Since PL emission arises from the recombination of these charge carriers, a lower PL intensity reflects more efficient charge separation. Among the composites, the 10% g-C_3N_4 sample exhibits the weakest PL signal, which corresponds well with its superior photocatalytic performance. This correlation supports the conclusion that suppressed electron-hole recombination, evidenced by lower PL emission, is a key factor contributing to the enhanced photocatalytic activity in Bi_2WO_6/g-C_3N_4 composites.

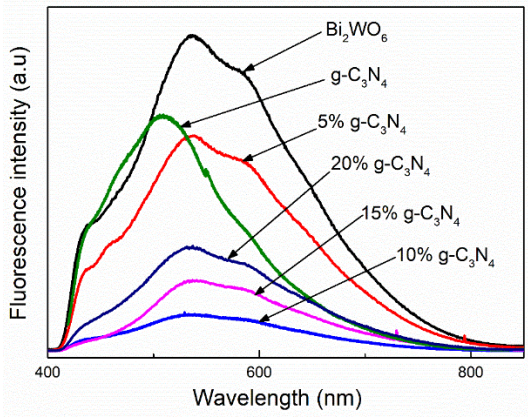

Figure 5. Photoluminescence (PL) spectra of pure g-C_3N_4, Bi_2WO_6/g-C_3N_4 composites with 5%, 10%, 15%, 20% g-C_3N_4, and pristine Bi_2WO_6

To elucidate the mechanism underlying the enhanced photocatalytic performance, we compared the photocatalytic activities and fabrication methods of various Bi_2WO_6/g-C_3N_4-based composites, as summarized in Table 3.

Table 3. Comparison of the photocatalytic performance and fabrication methods of Bi_2WO_6/g-C_3N_4-based composites

Composite materials	**Band gap (eV)**	**Surface area (m^2/g)**	**Preparation method**	**Enhancement activity compared to pure Bi_2WO_6**	**Photocatalytic mechanism**	**Reference**
C_3N_4 /Bi_2WO_6	2.63	42.2	Hydrothermal method	2.7	Heterojunction	[28]
Bi_2WO_6/g-C_3N_4	2.6	-	Hydrothermal method	1.94	Hetorojunction	[29]
C_3N_4 /Bi_2WO_6	2.54	-	Hydrothermal method	8.4	Z scheme	[30]
CdS QDs/Bi_2WO_6/g-C_3N_4	2.56	60.4	Hydrothermal method	8	Z scheme	[31]
Bi_2WO_6/g-C_3N_4	2.62	-	Hydrothermal method	6	Z-scheme	[32]
Bi_2WO_6/g-C_3N_4	2.5	-	Hydrothermal method	5	S-scheme	[33]
Bi_2WO_6/g-C_3N_4	2.7	20.6	Microwave assisted and Hydrothermal method	7	Z-scheme	This work

The results indicate that the composite containing 10 wt % g-C_3N_4-synthesized via a microwave-assisted hydrothermal method exhibits a degradation rate approximately seven times higher than that of pristine Bi_2WO_6. This enhancement is comparable to or exceeds the performance reported for other Z-scheme systems. In addition, PL measurements reveal significant suppression of PL emission intensity in this sample, suggesting more effective separation of photogenerated electron–hole pairs. These findings provide strong evidence supporting the formation of a Z-scheme heterojunction as the dominant charge-transfer pathway in our composite system.

The mechanism of photocatalytic enhancement can be interpreted based on possible charge-transfer models. Under visible-light irradiation, both Bi_2WO_6 and g-C_3N_4 absorb photons and generate electron-hole pairs via excitation from their valence bands (VB) to their conduction bands (CB). One commonly proposed mechanism is the type-II heterojunction, in which photoexcited electrons in the CB of g-C_3N_4 migrate to the CB of Bi_2WO_6, while holes in the VB of Bi_2WO_6 transfer to the VB of g-C_3N_4. This configuration facilitates charge separation but compromises the strong redox potentials of the individual components, typically leading to only moderate photocatalytic enhancement-approximately twofold relative to pure Bi_2WO_6 [28], [29]. In contrast, the Z-scheme heterojunction, illustrated in Figure 6, provides a more favorable charge-transfer pathway. In this configuration, electrons in the CB of Bi_2WO_6 recombine with holes in the VB of g-C_3N_4 at the interface, thereby retaining the high-energy electrons in the CB of g-C_3N_4 and the strongly oxidative holes in the VB of Bi_2WO_6. This selective recombination not only maintains the high redox potentials of both semiconductors but also effectively suppresses charge recombination. As a result, the Z-scheme architecture significantly boosts photocatalytic activity. Consistent with our findings, previous reports have shown that Z-scheme systems can achieve more than a sixfold enhancement in photocatalytic performance compared to pristine Bi_2WO_6 [30]-[33].

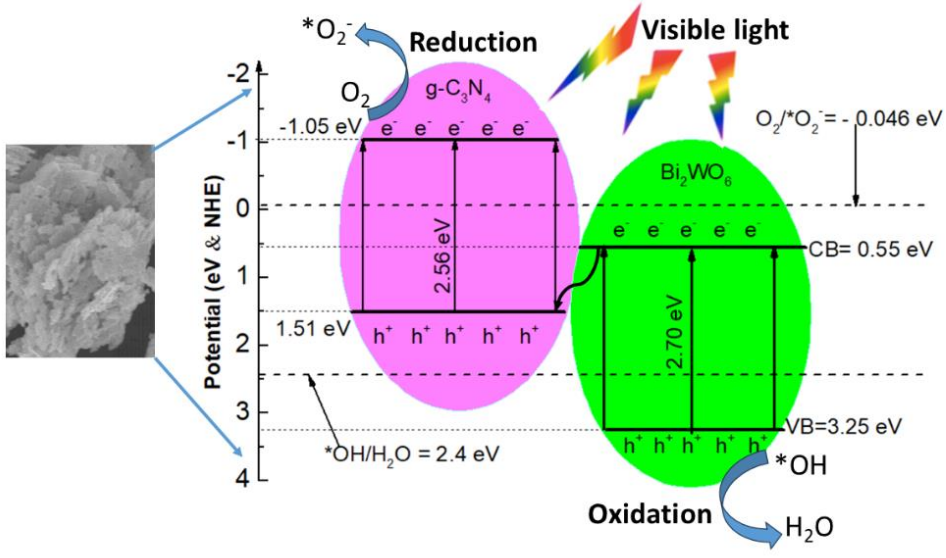

Figure 6. Proposed photocatalytic mechanism over the Bi_2WO_6/g-C_3N_4 composite

3. Conclusions

In this study, Bi_2WO_6/g-C_3N_4 composites with varying g-C_3N_4 contents were synthesized via a microwave-assisted hydrothermal method and systematically characterized. The incorporation of g-C_3N_4 significantly altered the morphology, optical absorption, and electronic structure of Bi_2WO_6, leading to an enhanced visible-light response and a reduced band-gap energy. Photoluminescence and photocatalytic analyses revealed that the composites exhibited suppressed electron-hole recombination and markedly improved RhB degradation compared with pristine Bi_2WO_6. Among the composites, the 10 % g-C_3N_4 sample demonstrated the highest activity, degrading RhB almost completely within 60 min-approximately seven times faster than pure Bi_2WO_6. The enhanced performance is attributed to the formation of a direct Z-scheme heterojunction between Bi_2WO_6 and g-C_3N_4, which promotes efficient charge separation while maintaining strong redox potentials. These findings highlight the potential of Bi_2WO_6/g-C_3N_4 composites as effective visible-light-driven photocatalysts for environmental remediation.

Acknowledgments. This research was funded by the Vietnam National Foundation for Science and Technology Development (NAFOSTED) under Grant No. 103.02-2021.80.

REFERENCES

[1] Wan G & Wang G, (2014). Synthesis of Bi_2WO_6 microspheres with visible-light-driven photocatalytic properties. *International Journal of Nanoscience,* 12. DOI: 10.1142/S0219581X1350035X.

[2] Yan Y, Wu Y, Yan Y, Guan W & Shi W, (2013). Inorganic-salt-assisted morphological evolution and visible-light-driven photocatalytic performance of Bi_2WO_6 nanostructures. *Journal of Physical Chemistry C*, 117, 20017-20028. DOI:10.1021/JP406574Y.

[3] Chen Y, Zhang L, Chen S, Sun S, Cheng H, Li S, Yu J, Ding B, & Yan J, (2024). Synthesis of Heteromorphic Bi_2WO_6 Films With an Interpenetrate 1D/2D Network Structure for Efficient and Stable Photocatalytic Degradation of VOCs. *Advanced Materials,* 36, 2407400. DOI:10.1002/ADMA.202407400.

[4] Rajan G, Rajput RB, Shaikh RS & Kale RB, (2025). Hydrothermally engineered highly active Bi_2WO_6 photocatalyst for the degradation of Rhodamine B, Bisphenol A and dye mixture under visible light irradiation. *Inorganic Chemistry Communications*, 177, 114430. DOI:10.1016/J.INOCHE.2025.114430.

[5] Yaghoobi-Rahni S, Younesi H, Bahramifar N, Yang H & Karimi-Maleh H, (2025). One-step hydrothermal process for fabrication of Bi_2WO_6/basic bismuth nitrate heterojunction with improved photocatalytic efficacy under visible light. J*ournal of Hazardous Materials Advances*, 17, 100624. DOI: 10.1016/J.HAZADV.2025.100624.

[6] Shad NA, Zahoor M, Bano K, Bajwa SZ, Amin N, Ihsan A, Soomro RA, Ali A, Imran Arshad M, Wu A, Iqbal MZ & Khan WS, (2017). Synthesis of flake-like bismuth tungstate (Bi_2WO_6) for photocatalytic degradation of coomassie brilliant

blue (CBB). *Inorganic Chemistry Communications,* 86, 213-217. DOI: 10.1016/J.INOCHE.2017.10.022.

[7] Nguyen DP, Luc HH, Chen XB, Kong MH, Wen HC & Chou WC, (2015). Study of photocatalytic activities of Bi_2WO_6 nanoparticles synthesized by fast microwave-assisted method. *Journal of Alloys and Compounds,* 647, 123-128. DOI: 10.1016/J.JALLCOM.2015.06.047.

[8] Shi J, Zhao T, Yang T, Pu K, Shi J, Zhou A, Li H, Wang S & Xue J, (2024). Z-scheme heterojunction photocatalyst formed by MOF-derived C-TiO_2 and Bi_2WO_6 for enhancing degradation of oxytetracycline: Mechanistic insights and toxicity evaluation in the presence of a single active species. *Journal of Colloid and Interface Science,* 665, 41-59. DOI: 10.1016/J.JCIS.2024.03.100.

[9] Qin Z, Zhu L, Ge X, Li C, Wang X & Liu X, (2025). Flower-spherical Ag-Bi_2WO_6 photocatalytic degradation of sulfamethazine. *Inorganic Chemistry Communications,* 171, 113618. DOI: 10.1016/J.INOCHE.2024.113618.

[10] Nguyen PH, Nguyen TQ, Vo TTN, Cao TM & Pham VV, (2025). Advanced oxidation processes over Fe-doped Bi_2WO_6 photocatalysts toward rhodamine B and cefalexin treatment. *Journal of Science: Advanced Materials and Devices,* 10(1), 100815. DOI: 10.1016/J.JSAMD.2024.100815.

[11] Nguyen DP, Luc HH, Pham VH, Tran QH, Chen XB & Chou WC, (2020). Photocatalytic activity enhancement of Bi_2WO_6 nanoparticles by Ag doping and Ag nanoparticles modification. *Journal of Alloys and Compounds*, 824, 153914. DOI: 10.1016/J.JALLCOM.2020.153914.

[12] Rana A, Sonu S, Soni V, Chawla A, Sudhaik A, Raizada P, Ahamad T, Thakur P, Thakur S & Singh P, (2025). Novel S-scheme derived Mo–Bi_2WO_6/WO_3/Biochar composite for photocatalytic removal of Methylene Blue dye. *Journal of Physics and Chemistry of Solids*, 196, 112385. DOI: 10.1016/J.JPCS.2024.112385.

[13] Yang ZL, Zeng HY, Xiong J, Peng DY & Liu SG, (2023). F-doped Bi_2WO_6 with rich oxygen vacancies for boosting photo-oxidation/reduction activity. *Colloids and Surfaces A: Physicochemical and Engineering Aspects*, 675 132035. DOI: 10.1016/J.COLSURFA.2023.132035.

[14] Luc HH, Nguyen DP, Peng H & Chen XB, (2018). High photocatalytic activity N-doped Bi_2WO_6 nanoparticles using a two-step microwave-assisted and hydrothermal synthesis. *Journal of Alloys and Compounds*, 744 228-233. DOI: 10.1016/J.JALLCOM.2018.02.094.

[15] Nguyen DP, Luc HH, Guo PC, Chen XB & Wu CC, (2017). Study of photocatalytic activities of Bi_2WO_6/$BiVO_4$ nanocomposites, *Journal of Sol-Gel Science and Technology,* 83, 640-646. DOI: 10.1007/S10971-017-4450-8.

[16] Segovia-Sandoval SJ, Mendoza-Mendoza E, Jacobo-Azuara A, Jiménez-López BA & Hernández-Arteaga AC, (2024). Highly efficient visible-LED-driven photocatalytic degradation of tetracycline and rhodamine B over Bi_2WO_6/$BiVO_4$ heterostructures decorated with silver and graphene synthesized by a novel green method. *Environmental Science and Pollution Research*, 31(28), 39945-39960. DOI: 10.1007/S11356-023-27731-6.

[17] Shen T, Zeng D, Liu Z, Hu Y, Tian Y, Song J, Yang T, Guan R & Zhou C, (2024). S-scheme Bi/Bi_2WO_6/TiO_2 nanofiber photocatalyst for efficient degradation of sulfamethoxazole. *Separation and Purification Technology,* 351 128130. DOI: 10.1016/J.SEPPUR.2024.128130.

[18] Kumar A, Singla Y, Sharma M, Bhardwaj A & Krishnan V, (2022). Two dimensional S-scheme Bi_2WO_6–TiO_2–Ti_3C_2 nanocomposites for efficient degradation of organic pollutants under natural sunlight. *Chemosphere*, 308, 136212. DOI: 10.1016/J.CHEMOSPHERE.2022.136212.

[19] Dai W, Yu J, Deng Y, Hu X, Wang T & Luo X, (2017). Facile synthesis of MoS_2/Bi_2WO_6 nanocomposites for enhanced CO_2 photoreduction activity under visible light irradiation. *Applied Surface Science,* 403, 230-239. DOI: 10.1016/J.APSUSC.2017.01.171.

[20] Zhang B, Liu Y, Wang D, He W, Fang X, Zhao C, Pan J, Liu D, Liu S, Chen T, Zhao L & Wang J, (2025). Nanoengineering construction of g-C_3N_4/Bi_2WO_6 S-scheme heterojunctions for cooperative enhanced photocatalytic CO2 reduction and pollutant degradation. *Separation and Purification Technology*, 354, 128893. DOI: 10.1016/J.SEPPUR.2024.128893.

[21] Li H, Li N, Wang M, Zhao B & Long F, (2018). Synthesis of novel and stable g-C_3N_4-Bi_2WO_6 hybrid nanocomposites and their enhanced photocatalytic activity under visible light irradiation. *Royal Society Open Science*, 5(3), DOI: 10.1098/RSOS.171419.

[22] Lian X, Xue W, Dong S, Liu E, Li H & Xu K, (2021). Construction of S-scheme Bi_2WO_6/g-C_3N_4 heterostructure nanosheets with enhanced visible-light photocatalytic degradation for ammonium dinitramide. *Journal of Hazardous Materials*, 412, 125217. DOI: 10.1016/J.JHAZMAT.2021.125217.

[23] Qi S, Zhang R, Zhang Y, Liu X & Xu H, (2021). Preparation and photocatalytic properties of Bi_2WO_6/g-C_3N_4. *Inorganic Chemistry Communications*, 132, 108761. DOI: 10.1016/J.INOCHE.2021.108761.

[24] Masoud A, Ahmed MA, Kühn F & Bassioni G, (2023). Nanosheet g-C_3N_4 enhanced by Bi_2MoO_6 for highly efficient photocatalysts toward photodegradation of Rhodamine-B dye. *Heliyon*, 9(11). DOI: 10.1016/J.HELIYON.2023.E22342.

[25] Cao D, Su N, Wang X, Wang X, Xu C, Liu Z, Li J & Lu C, (2024). Construction of unique floating Bi_2WO_6/g-C_3N_4 S-scheme heterojunction to promote photocatalytic activity. *Journal of Environmental Chemical Engineering,* 12(3), 112939. DOI: 10.1016/J.JECE.2024.112939.

[26] Wen J, Xie J, Chen X & Li X, (2017). A review on g-C_3N_4-based photocatalysts. *Applied Surface Science*, 391, 72-123. DOI: 10.1016/J.APSUSC.2016.07.030.

[27] Ge L, Han C & Liu J, (2011). Novel visible light-induced g-C_3N_4/Bi_2WO_6 composite photocatalysts for efficient degradation of methyl orange. *Applied Catalysis B: Environment and Energy*, 108, 100-107. DOI: 10.1016/J.APCATB.2011.08.014.

[28] Wang J, Tang L, Zeng G, Deng Y, Liu Y, Wang L, Zhou Y, Guo Z, Wang J & Zhang C, (2017). Atomic scale g-C_3N_4/Bi_2WO_6 2D/2D heterojunction with enhanced

photocatalytic degradation of ibuprofen under visible light irradiation. *Applied Catalysis B: Environment and Energy*, 209, 285-294. DOI: 10.1016/J.APCATB.2017.03.019.

[29] Qi S, Zhang R, Zhang Y, Liu X & Xu H, (2021). Preparation and photocatalytic properties of Bi_2WO_6/g-C_3N_4. *Inorganic Chemistry Communications*, 132, 108761. DOI: 10.1016/J.INOCHE.2021.108761.

[30] Zhang B, Liu Y, Wang D, He W, Fang X, Zhao C, Pan J, Liu D, Liu S, Chen T, Zhao L & Wang J, (2025). Nanoengineering construction of g-C_3N_4/Bi_2WO_6 S-scheme heterojunctions for cooperative enhanced photocatalytic CO_2 reduction and pollutant degradation. *Separation and Purification Technology*, 354, 128893. DOI: 10.1016/J.SEPPUR.2024.128893.

[31] Du Y, Li L, Tang Y, Li J, Guo Q & Yue G, (2025). Effective degradation of multiple antibiotics by 0D/3D/2D dual Z-heterojunction photocatalyst CdS QDs/Bi_2WO_6/g-C_3N_4 and study of degradation mechanism. *Applied Surface Science,* 697, 163004. DOI: 10.1016/J.APSUSC.2025.163004.

[32] Xiao X, Wei J, Yang Y, Xiong R, Pan C & Shi J, (2016). Photoreactivity and Mechanism of g-C_3N_4 and Ag Co-Modified Bi_2WO_6 Microsphere under Visible Light Irradiation. *ACS Sustainable Chemistry & Engineering Journal*, 4(6), 3017-3023. DOI: 10.1021/ACSSUSCHEMENG.5B01701.

[33] Cao D, Su N, Wang X, Wang X, Xu C, Liu Z, Li J & Lu C, (2024). Construction of unique floating Bi_2WO_6/g-C_3N_4 S-scheme heterojunction to promote photocatalytic activity. *Journal of Environmental Chemical Engineering*, 12(3), 112939. DOI: 10.1016/J.JECE.2024.112939.